https://doi.org/10.5194/egusphere-2025-5432
Preprint. Discussion started: 18 November 2025

Global CO emissions and drivers of atmospheric CO trends constrained by MOPITT satellite observations

Zhaojun Tang[1,2], Panpan Yang[3], Kazuyuki Miyazaki[4], John Worden[4], Helen Worden[5], Daven K. Henze[6], Dylan B. A. Jones[7] and Zhe Jiang[3]*

[1]Key Laboratory of Atmospheric Optics, Anhui Institute of Optics and Fine Mechanics, HIPS, Chinese Academy of Sciences, Hefei, Anhui, 230031, China.
[2]School of Earth and Space Sciences, University of Science and Technology of China, Hefei, Anhui, 230026, China.
[3]Institute of Surface–Earth System Science, School of Earth System Sciences, Tianjin University, Tianjin, 300072, China.
[4]Jet Propulsion Laboratory, California Institute of Technology, Pasadena, CA, 91009, USA.
[5]Atmospheric Chemistry Observations and Modeling Laboratory, National Center for Atmospheric Research, Boulder, CO, 80301, USA.
[6]Department of Mechanical Engineering, University of Colorado, Boulder, CO, 80309, USA.
[7]Department of Physics, University of Toronto, Toronto, ON, M5S 1A7, Canada.

*Correspondence to: Zhe Jiang (zhejiang@tju.edu.cn)

Abstract

Carbon monoxide (CO), an important atmospheric pollutant produced from incomplete combustion and hydrocarbon oxidation, significantly influences atmospheric chemistry and air quality. Accurate quantification of its global emissions and the underlying drivers of atmospheric trends is essential for understanding and improving global environmental conditions. Using 20 years (2003-2022) of satellite observations from the Measurement of Pollution in the Troposphere (MOPITT) instrument, here we analyze changes in global CO emissions and atmospheric concentrations. The a posteriori simulations show improved consistency with independent surface and aircraft measurements compared to the a priori simulations. Sensitivity analyses further confirm that inferred emissions remain robust against uncertainties associated with satellite vertical sensitivity and variations in hydroxyl radical (OH) concentrations. Our results indicate a substantial decline in global anthropogenic CO emissions of 14-17% (approximately 85-110 Tg) over the two-decade period, largely driven by reductions

https://doi.org/10.5194/egusphere-2025-5432
Preprint. Discussion started: 18 November 2025

in the United States, Europe, and eastern China. In contrast, biomass burning emissions exhibited strong interannual variability, with recent increases in Northern Hemisphere high-latitude forests. A key finding is that rising biomass burning emissions have offset about 37% of the global anthropogenic emission reduction (47% in the Northern Hemisphere alone), underscoring the considerable moderating influence of wildfires on atmospheric composition trends. This study provides a comprehensive assessment of global CO emissions and the mechanisms governing atmospheric CO trends, offering a scientific basis for integrated policies addressing both climate change and air pollution.

1. Introduction

Carbon monoxide (CO) is a key atmospheric pollutant produced from incomplete combustion and the oxidation of hydrocarbons. As the main sink for the hydroxyl radical (OH), CO critically influences the oxidative capacity of the atmosphere (Zhao et al., 2020; Tan et al., 2022), and is an important precursor for tropospheric ozone (Whaley et al., 2015; Hu et al., 2024). With a chemical lifetime of approximately one to two months, CO is frequently employed as a valuable tracer for elucidating variations in anthropogenic activities and biomass burning, providing critical insights into the long-range transport of atmospheric constituents (Tang et al., 2019; Buchholz et al., 2022; Smoydzin and Hoor, 2022). Accurate quantification of global CO emissions and a clear understanding of the drivers behind its atmospheric trends are therefore essential for formulating effective policies to address the challenges of air quality and climate change.

The advent of long-term satellite observations has revolutionized our ability to monitor global CO distributions (Warner et al., 2013; Worden et al., 2013; Hedelius et al., 2021). This data has enabled a shift from short-term, regional emission estimates (Arellano et al., 2004; Heald et al., 2004; Kopacz et al., 2010) to analyses of decadal-scale changes. Numerous studies

https://doi.org/10.5194/egusphere-2025-5432
Preprint. Discussion started: 18 November 2025

have leveraged these records to report substantial declines in anthropogenic CO emissions (Fortems-Cheiney et al., 2011; Jiang et al., 2017; Miyazaki et al., 2020), especially across the Northern Hemisphere, contributing to improved air quality. However, a critical and emerging challenge is to disentangle the competing influences on atmospheric CO concentrations. While anthropogenic emissions are generally decreasing due to pollution control measures, biomass burning emissions exhibit strong interannual variability and a growing sensitivity to climate change. An important unanswered question is to what extent the recent intensification of wildfires, particularly in high-latitude forests (Jain et al., 2024; Jones et al., 2024), is offsetting the gains achieved from anthropogenic emission reductions. This has profound implications, as CO shares common combustion sources with major greenhouse gases like methane (CH_4) and carbon dioxide (Worden et al., 2017; Zheng et al., 2023).

Constraining global emissions and robustly attributing observed concentration trends require the application of sophisticated inverse modeling approaches. These methods, which include ensemble-based techniques (e.g., the ensemble Kalman filter) and variational methods (e.g., four-dimensional variational, 4D-Var, data assimilation), provide powerful frameworks for optimizing emission estimates by reconciling model simulations with satellite observations, while accounting for complex atmospheric transport and chemistry (Müller et al., 2018; Miyazaki et al., 2020; Jiang et al., 2025). Among these, the 4D-Var data assimilation, implemented within chemical transport models like GEOS-Chem and its adjoint (Henze et al., 2007), has been widely and successfully applied to constrain CO emissions (Kopacz et al., 2010; Jiang et al., 2015b; Tang et al., 2023), owing to its strengths in handling nonlinear constraints and providing computationally efficient gradients. However, long-term multi-decadal trend analyses based on this system has often been hindered by limitations such as inconsistent meteorological inputs across years and the use of outdated a priori emission inventories (Jiang et al., 2017; Qu et al., 2022).

https://doi.org/10.5194/egusphere-2025-5432
Preprint. Discussion started: 18 November 2025

To address these limitations, we employ a recent extension of the GEOS-Chem adjoint model (Tang et al., 2023) that features support for consistent MERRA-2 meteorological data and modern emission inventories via the HEMCO emissions component (Keller et al., 2014; Lin et al., 2021). By assimilating MOPITT (Measurements of Pollution in the Troposphere) observations from 2003 to 2022, this study aims to provide an analysis with the following specific objectives: (1) to quantify the long-term evolution of global CO emissions; (2) to attribute the observed trends in atmospheric CO concentrations to changes in emissions and meteorological variations, in particularly, the effect of increasing biomass burning emissions on atmospheric CO decline driven by anthropogenic reductions; and (3) to evaluate the sensitivity of inferred emissions to uncertainties in satellite vertical sensitivity and OH concentrations. By doing so, this work aims to improve the understanding of key drivers behind atmospheric CO changes and offer a refined emission inventory to support future climate and air quality policies.

The paper is structured as follows: Section 2 describes the methodology, including the assimilation framework, observational data, and the design of sensitivity experiments. Section 3 presents the results on the long-term emission trends, the robustness tests, and the attribution of concentration changes. Conclusions are provided in Section 4.

2. Methodology and Data

2.1 Assimilation framework

We utilize the adjoint of the GEOS-Chem model (version 35n) with extended support for MERRA-2 meteorological data and HEMCO emission inventories. The analysis is conducted at a horizontal resolution of 2°×2.5° with 47 vertical levels (MERRA-2) and employs a CO-only simulation (tagged-CO mode). Two types of archived OH fields are used in this study: fixed monthly OH fields for 2013 from the GEOS-Chem full chemistry simulation (Fisher et

https://doi.org/10.5194/egusphere-2025-5432
Preprint. Discussion started: 18 November 2025

al., 2017), and variable monthly OH fields for 2005-2020 from the Tropospheric Chemistry Reanalysis version 2 (TCR-2, Miyazaki et al. (2020)). The TCR-2 OH fields have been validated against various aircraft observations and show generally good agreement (Miyazaki et al., 2020). The interannual variability of global mean tropospheric OH concentrations from TCR-2 is illustrated in Fig. S2 (see the SI).

The global default anthropogenic emission inventory is the CEDS (Community Emissions Data System) (Hoesly et al., 2018). Regional emissions are replaced as follows: MIX (Li et al., 2017) over Asia, NEI 2016 (National Emissions Inventory) over the United States, DICE_AFRICA and EDGARv4.3 over Africa, and APEI over Canada. Biogenic emissions are simulated using the Model of Emissions of Gases and Aerosols from Nature, version 2.0 (MEGANv2.0, Guenther et al. (2006)). Biomass burning emissions are based on the Global Fire Emissions Database version 4 (GFED4, van der Werf et al. (2010)). The distribution of the annual mean CO emissions from 2003 to 2022 is shown in Figs. 1a-c. The annual global sources are 536.3 Tg yr^{-1} from anthropogenic emissions, 312.5 Tg yr^{-1} from biomass burning, and 623 Tg yr^{-1} from the oxidation of biogenic VOCs.

The objective of the 4D-Var approach is to minimize the difference between simulations and observations by minimizing the cost function (Henze et al., 2007):

$$J(\boldsymbol{x}) = \sum_{i=1}^{N}(\boldsymbol{F}_i(\boldsymbol{x}) - \boldsymbol{z}_i)^T \boldsymbol{S}_{\Sigma}^{-1}(\boldsymbol{F}_i(\boldsymbol{x}) - \boldsymbol{z}_i) + \gamma(\boldsymbol{x} - \boldsymbol{x}_a)^T \boldsymbol{S}_a^{-1}(\boldsymbol{x} - \boldsymbol{x}_a) \quad (1)$$

where $\boldsymbol{x}$ is the state vector of CO emissions, N is the number of observations distributed in time over the assimilation period, $\boldsymbol{z}_i$ are the MOPITT CO observations, and $\boldsymbol{F}(\boldsymbol{x})$ is the forward model. Error estimates are assumed to be Gaussian: $\boldsymbol{S}_{\Sigma}$ is the observational error covariance, which combines a 10% uniform error and the MOPITT CO retrieval error covariance; and $\boldsymbol{S}_a$ is the a priori error covariance. Here the combustion-related CO sources (fossil fuel, biofuel, and biomass burning) and the oxidation source from biogenic VOCs are combined, with a uniform a priori error of 50% assumed. The CO source from CH_4 oxidation

https://doi.org/10.5194/egusphere-2025-5432
Preprint. Discussion started: 18 November 2025

is optimized separately as an aggregated global source, with the a priori uncertainty of 25%. The cost function is minimized by iteratively adjusting the CO emissions using the quasi-Newton gradient-based optimization L-BFGS-B algorithm (Zhu et al., 1997) and the adjoint gradients:

$$\nabla_{\boldsymbol{x}} J(\boldsymbol{x}) = \sum_{k=1}^{N} \left[2 \left(\frac{\partial \boldsymbol{F}_i}{\partial \boldsymbol{x}} \right)^{\boldsymbol{T}} \boldsymbol{S}_{\Sigma}^{-1} (\boldsymbol{F}_i(\boldsymbol{x}) - \boldsymbol{z}_i) \right] + 2\gamma (\boldsymbol{x} - \boldsymbol{x}_a)^T \boldsymbol{S}_a^{-1} \quad (2)$$

The LOGX2 method (Jiang et al., 2015a; Jiang et al., 2017) is employed to improve the reduction of negative gradients.

Following Jiang et al. (2017), we applied a two-step approach to mitigate the influence of systematic biases in the model simulations. First, a sequential Kalman filter (Todling and Cohn, 1994; Tang et al., 2022) was used to assimilate MOPITT CO observations, providing optimized CO concentration fields with lower bias. As illustrated in Fig. 2a, the GEOS-Chem model driven by the original monthly CO initial conditions and a priori emission inventories (referred to as GC-original) substantially underestimated column CO concentrations by approximately 30–40% (mean bias = -39.4 × 10^{16} molecules cm^{-2}; Table 1). In contrast, simulations using the monthly CO initial conditions derived from the sequential Kalman filter together with a priori emissions (GC-a priori) showed markedly improved agreement with MOPITT observations (Fig. 2b), reducing the mean bias to about 10% (mean bias = -9.7 × 10^{16} molecules cm^{-2}). Similarly, the use of optimized monthly CO initial conditions led to considerable improvement in model performance against independent surface and aircraft measurements (Table 1). The mean bias decreased from -20.1 ppb (GC-original) to -2.4 ppb (GC-a priori) for WDCGG surface observations; from -18.9 ppb to -3.8 ppb for HIPPO aircraft data; and from -16.2 ppb to -3.4 ppb for ATOM aircraft measurements. These results suggest that the substantial negative biases seen in Fig. 2a largely originate from the accumulation of biases over preceding months.

Furthermore, ocean scenes (red grids in Fig. S3) were defined as land boundary conditions.

https://doi.org/10.5194/egusphere-2025-5432
Preprint. Discussion started: 18 November 2025

The optimized CO fields from the Kalman filter were used to update CO concentrations over the ocean at hourly intervals during the forward simulation within the 4D-Var process. Meanwhile, the 4D-Var system constrained CO emissions over land without modifying oceanic CO distributions. As demonstrated by Jiang et al. (2017), the use of optimized CO land boundary conditions in 4D-Var assimilation effectively reduces systematic biases associated with long-range transport. By adopting this two-step assimilation framework, the inversion focuses on optimizing fresh continental CO emissions, while reducing the influence of uncertainties arising from transport and chemical processes, which tend to exhibit larger systematic biases. Consequently, the a posteriori CO emissions estimated in this study are expected to be lower than those derived without adjustments to the initial and boundary CO conditions. This reflects both the specific inverse modeling setup and a possible underestimation in our a posteriori emission estimates, attributable to the emphasis on constraining fresh continental CO sources.

Based on this assimilation framework, three sets of CO emission inversion experiments are designed:

(1) Col-FixOH: uses MOPITT CO column concentration data with default OH fields fixed in 2013.

(2) Prof-FixOH: uses MOPITT CO profile data with default OH fields fixed in 2013.

(3) Col-VarOH: uses MOPITT CO column concentration data with variable OH fields from the TCR-2 tropospheric chemistry reanalysis.

By comparing the results of Col-FixOH and Prof-FixOH, the influence of different MOPITT CO observation types on CO source estimates can be assessed. Similarly, comparing Col-FixOH and Col-VarOH allows for evaluation of the impact of different OH fields on CO source estimates.

2.2 MOPITT CO measurements

https://doi.org/10.5194/egusphere-2025-5432
Preprint. Discussion started: 18 November 2025

The MOPITT instrument was launched on December 18, 1999, aboard the NASA Terra spacecraft. The satellite follows a sun-synchronous polar orbit at 705 km altitude, crossing the equator at 10:30 local time. The instrument made measurements over a 612 km cross-track scan, with a footprint of 22 km × 22 km. The MOPITT data used in this study are from the joint retrieval (version 9J) of CO, which combines thermal infrared (TIR, 4.7μm) and near-infrared (NIR, 2.3μm) radiances using an optimal estimation approach (Worden et al., 2010; Deeter et al., 2022). The retrieved volume mixing ratios are reported as layer averages across 10 pressure levels (surface, 900, 800, 700, 600, 500, 400, 300, 200, and 100 hPa). The relationship between the retrieved CO profile and the true atmospheric state is expressed as:

$$\hat{\boldsymbol{z}} = \boldsymbol{z}_a + \boldsymbol{A}(\boldsymbol{z} - \boldsymbol{z}_a) + \boldsymbol{G}\boldsymbol{\epsilon} \tag{3}$$

where $\boldsymbol{z}_a$ is the MOPITT a priori CO profile, $\boldsymbol{z}$ is the true atmospheric state, $\boldsymbol{G}\boldsymbol{\varepsilon}$ represents the retrieval error, and $\boldsymbol{A} = \partial\hat{\boldsymbol{z}}/\partial\boldsymbol{z}$ is the MOPITT averaging kernel matrix, indicating the sensitivity of the retrieval to the actual atmospheric CO. We exclude MOPITT data with CO column amounts less than 5×10^{17} molecules cm^{-2} and those with low cloud observations. Since the NIR channel relies on reflected solar radiation, only daytime data are considered.

2.3 Aircraft and surface CO measurements

The HIAPER Pole-to-Pole Observations (HIPPO, Wofsy and HIPPO Science Team (2011)) were conducted using the Gulfstream V aircraft from 2009 to 2011. The flights primarily covered the Pacific Ocean, spanning latitudes from 67°S to 87°N, with continuous sampling from 0.2 to 12 km altitude. The Atmospheric Tomography Mission (ATom, Wofsy and Atom Science Team (2018)) used the DC-8 aircraft from 2016 to 2018. ATom covered similar altitude and latitudinal ranges as HIPPO but with broader spatial coverage, particularly over the Atlantic Ocean. For HIPPO, a total of 687 CO profiles from five missions were used directly. For ATom, CO measurements during continuous ascents and descents were used to construct 523 CO profiles from four missions. Surface CO measurements from the World Data

https://doi.org/10.5194/egusphere-2025-5432
Preprint. Discussion started: 18 November 2025

Centre for Greenhouse Gases (WDCGG) are also included in this analysis. The WDCGG, operated by the Japan Meteorological Agency under the World Meteorological Organization's Global Atmosphere Watch (GAW) program, collects, archives, and distributes atmospheric greenhouse gas data, including CO, contributed by various institutions worldwide.

3. Results and Discussion

3.1 Evaluation of assimilation system performance

Before presenting the estimated emission trends and their drivers, we first evaluate the performance of our assimilation system. The evaluation involves comparing modeled CO concentrations from the GC-original, GC-a priori, and the a posteriori simulations (Col-FixOH, Prof-FixOH, Col-VarOH) over the period 2003-2022 against MOPITT satellite retrievals, as well as independent surface observations from WDCGG and aircraft measurements from HIPPO and ATom. As summarized in Table 1, the a posteriori simulations exhibit mean biases relative to MOPITT observations ranging from -5.1 to -7.3 × 10^{16} molecules cm^{-2}. These values are notably lower than the biases in the GC-a priori simulation (-9.7 × 10^{16} molecules cm^{-2}) and the GC-original simulation (-39.4 × 10^{16} molecules cm^{-2}). Similarly, for the HIPPO aircraft observations, the a posteriori simulations show mean biases between -2.5 and -2.1 ppb, improved compared to the GC-a priori (-3.8 ppb) and GC-original (-18.9 ppb) simulations. For ATom aircraft data, the a posteriori mean biases range from -2.9 to -1.6 ppb, also lower than those from the GC-a priori (-3.4 ppb) and GC-original (-16.2 ppb) simulations. These results confirm that the a posteriori emission estimates lead to improved agreement with atmospheric CO observations.

In the case of surface CO concentrations, the a posteriori simulations yield mean biases between 0.4 and 1.8 ppb relative to WDCGG observations (Table 1), which are reduced compared to the GC-a priori (-2.4 ppb) and GC-original (-20.1 ppb) simulations. This supports

https://doi.org/10.5194/egusphere-2025-5432
Preprint. Discussion started: 18 November 2025

the conclusion that the assimilation improves the representation of surface-level CO. It is worth noting that the a posteriori simulations tend to slightly overestimate surface concentrations relative to WDCGG data, while generally underestimating CO in the free troposphere according to MOPITT and aircraft observations. This systematic pattern may be attributable to uncertainties in convective transport parameterizations within the model. Overall, the enhanced consistency between the a posteriori simulations and multiple independent observation platforms demonstrates the capability of our assimilation system to effectively constrain CO emissions. Given this confidence in the system's performance, we now present the central findings of this study: the long-term evolution of CO emissions as derived from the assimilation constraints.

3.2 Long-term evolution of global CO emissions

3.2.1 Anthropogenic CO emissions: global decline and regional differentiation

At the global scale, anthropogenic CO emissions were 7-14% higher than the a priori estimate (Figs. 1d, 1g, 1j and Table 2) showing a clear declining trend superimposed with notable interannual fluctuations (Fig. 3f and Table S1). Under the Col-FixOH configuration, global emissions from 2003 to 2022 ranged from 546.1 to 654.1 Tg yr^{-1}, with a multi-year average of approximately 610 Tg yr^{-1} and a total reduction of about 17%; Similar ranges and reduction magnitudes (14-17%) were observed under the Prof-FixOH and Col-VarOH configurations. As shown in Fig. 4a, negative trends (blue) were concentrated in three major industrialized regions: eastern North America, Europe, and eastern China, forming a distinct "reduction belt". These regions collectively accounted for over 65% of global anthropogenic CO emissions, and their systematic reductions constituted the principal driver of the global downward trend. In contrast, positive trends (red) were primarily distributed in northern India

https://doi.org/10.5194/egusphere-2025-5432
Preprint. Discussion started: 18 November 2025

(increases of 15.2-22.3%) and Central Africa, corresponding to rapid urbanization and industrialization processes.

Developed economies exhibited continuous decreases with distinct phases (Figs. 3a-b). In the United States (US), emissions declined rapidly from 2003 to 2009, followed by a period of slower reduction. Over the entire period (2003-2022), US CO emissions decreased at rates of 2.0-2.2 Tg yr^{-1}, resulting in a cumulative reduction of 46-49% (Table S1). This phased reduction pattern is consistent with the diminishing marginal effects of widespread transportation control technologies, as supported by independent studies (Elguindi et al., 2020; Miyazaki et al., 2020). European CO emissions showed a similar trend (a cumulative reduction of 32-34% in 2003-2022), with an average reduction rate of approximately 1.44 Tg yr^{-1} from 2003 to 2014, slowing after 2015. This finding differs slightly from that of Fortems-Cheiney et al. (2024), a discrepancy possibly attributable to differences in the processing of initial and boundary CO conditions (e.g., the use of climatological CO concentrations in Fortems-Cheiney et al. (2024)).

China's CO emissions demonstrated a distinct turning point from growth to decline (Fig. 3c). The evolution can be divided into four stages: (1) a growth period until 2007, reaching a peak; (2) a sharp decline of approximately 7% during the 2008 global financial crisis; (3) a temporary rebound from 2009 to 2011 under economic stimulus policies; and (4) a continuous decline phase after 2011. From 2003 to 2022, anthropogenic CO emissions from eastern China decreased at an average rate of 3.0-4.0 Tg yr^{-1} (Table 2), with a cumulative reduction of 23-32% (Table S1). This evolution is corroborated by multiple studies: Zhao et al. (2012) and Xia et al. (2016) confirmed the transformation of China's CO emission trend around 2007, attributing it to improved energy efficiency and emission control regulations; Lin and McElroy (2011) and Tong et al. (2016) emphasized the significant suppressive effect of the 2008 global economic recession; and Zheng et al. (2018) quantified a 27% reduction in CO emissions

https://doi.org/10.5194/egusphere-2025-5432
Preprint. Discussion started: 18 November 2025

between 2010 and 2017. Notably, the emission reduction rate accelerated during 2019-2022 (4.8-8.3 Tg yr^{-1}), reflecting not only the short-term impact of the COVID-19 pandemic but also the long-term cumulative effects of clean air policies and energy structure transformation.

In contrast, India exhibited a consistent growth trend in CO emissions, with an average annual increase of 0.5-0.8 Tg yr^{-1}. This growth was primarily driven by rapid industrialization and urbanization, particularly from coal and biomass fuel combustion in the residential sector in earlier years, and from the industrial and transportation sectors more recently (Kurokawa and Ohara, 2020). Comparisons with the CEDS inventory (Hoesly et al., 2018; Wang et al., 2022) indicate that India's anthropogenic emissions of major air pollutants like NO_x, CO, and NMVOCs have increased at a much faster rate than in other regions, reflecting sustained growth in fuel consumption across its industrial, energy, and transport sectors.

This regional analysis underscores the close association between CO emission evolution and stages of economic development, the intensity of policy interventions, and technological pathway choices. Developed, post-industrialized economies achieved continuous reductions through mature environmental policies. China, as a rapidly developing emerging economy, exhibited a transition consistent with an environmental Kuznets curve; India, in an accelerated industrialization phase, continues to show emission growth, though with emerging signs of policy intervention.

3.2.2 Biomass burning emissions: high variability and climate-driven characteristics

Globally, biomass burning CO emissions were 4-11% higher than the a priori estimate (Figs. 1e, 1h, 1k and Table 3). In contrast to the clear decline of anthropogenic emissions, biomass burning CO emissions exhibited high interannual variability without a significant long-term trend (Fig. 5). Under the Col-FixOH configuration, global emissions from 2003 to 2022 ranged from 277.4 to 477.9 Tg yr^{-1}, averaging 342 Tg yr^{-1} (Table S1). The interannual variability (standard deviation of 41.7 Tg yr^{-1}) far exceeded any secular trend, underscoring the

https://doi.org/10.5194/egusphere-2025-5432
Preprint. Discussion started: 18 November 2025

high sensitivity of biomass burning to climatic conditions and ecosystem states. Spatial analysis revealed a pronounced latitudinal differentiation (Figs. 4d-f). Positive trends (red) were concentrated in Northern Hemisphere high-latitude coniferous forests, while negative trends (blue) dominated tropical and subtropical regions. This pattern is consistent with the "global fire emission geographic reconstruction" observed by Zheng et al. (2023), reflecting the differential impacts of climate change across latitudinal zones.

Emissions from North American and Asian high-latitude coniferous forest regions increased dramatically. In 2021, CO emissions from boreal North America reached 52.2-91.9 Tg, an increase of 189-434% compared to 2003; emissions from boreal Asia increased by 48-117% over the same period. These two regions accounted for 39-51% of global total biomass burning emissions in 2021, reaching the highest level during the study period. This latitudinal amplification of emissions aligns with observations that carbon emission density from boreal forest fires is 4-10 times higher than from grasslands (Zheng et al., 2021), explaining the substantial increase despite potential decreases in global burned area. Furthermore, climate warming has led to extended fire seasons and increased frequency of extreme fire weather events (Justino et al., 2021). The record-breaking emissions in 2021 were triggered by severe concurrent droughts across North America and Eurasia (Zheng et al., 2023).

South American biomass burning CO emissions showed a long-term decrease but with significant interannual fluctuations (Fig. 5c), with high emission periods in 2004-2007, 2010, and 2019-2022. The trend shift in CO emissions after 2013 can be linked to changes in policy enforcement (Silva Junior et al., 2021), combustion efficiency (Bloom et al., 2015) and climate variability (Hooghiemstra et al., 2012; Jolly et al., 2015). In Africa, the overall trend of biomass burning CO emissions was not significant (Fig. 5d), but pronounced regional differentiation occurred (Fig. 4d-f), with increases in central Africa and decreases in surrounding areas, consistent with the "strong contrast" pattern observed by Andela et al. (2017). Emission

https://doi.org/10.5194/egusphere-2025-5432
Preprint. Discussion started: 18 November 2025

patterns in Southeast Asia and Australia highlighted their high sensitivity to large-scale climate oscillations. Major fire events in Indonesia in 2006, 2009, 2015, and 2019 were closely linked to El Niño-induced droughts (Page, 2009; Field et al., 2016; Huijnen et al., 2016). Australia's extreme fires in 2019 resulted from compound extreme climate conditions influenced by the El Niño-Southern Oscillation, the Southern Annular Mode, and the Indian Ocean Dipole (Deb et al., 2020).

3.2.3 Difference between combustion and biogenic NMVOC sources

CO from combustion sources in the Northern Hemisphere showed strong regional differentiation (Figs. 4j-l), reflecting a dynamic redistribution between declining anthropogenic sources and increasing biomass burning sources. Positive trends were densely distributed in high-latitude regions, mainly due to climate-driven increases in wildfires; Negative trends dominated mid-to-low latitude industrialized areas. Tropical regions showed a mixed pattern, while the Southern Hemisphere exhibited generally weaker trends. This spatial heterogeneity confirms a net global decrease in combustion-related CO, revealing a clear contrast between increases at high northern latitudes and decreases at mid-latitudes, reflecting the compound influences of climate change and policy interventions.

In contrast, CO produced from the oxidation of biogenic VOCs remained relatively stable from 2003 to 2022 (Fig. 4g-i). This stability aligns with findings by Messina et al. (2016), suggesting that global-scale biogenic VOC emissions are less sensitive to short-term climate and land cover changes. The global stability of biogenic VOC-derived CO is important for atmospheric chemistry, as these compounds are key reactants for OH radicals and play a regulatory role in atmospheric oxidation capacity. This stable background provides a crucial baseline for understanding changes in atmospheric oxidation processes. The weaker trends compared to those reported by Jiang et al. (2017) may be associated with our use of continuous MERRA-2 meteorological data, which enhances consistency in long-term analysis.

https://doi.org/10.5194/egusphere-2025-5432
Preprint. Discussion started: 18 November 2025

3.3 Impacts of systematic errors on inferred CO emissions

3.3.1 Impacts of vertical sensitivity of satellite retrievals

The MOPITT instrument provides observations for both CO total column and vertical profile. The degrees of freedom for signal (DFS) for MOPITT multi-spectral profile retrievals (TIR+NIR) is approximately 1.5-2.0 over land, reducing to about 1.0 when converted to a total column (Worden et al., 2010). The discrepancy between a posteriori emission estimates constrained by CO column (Col-FixOH) and profile (Prof-FixOH) data helps evaluate the influence of systematic errors associated with the vertical sensitivity of the satellite retrievals (Tang et al., 2024). This comparison also aids in understanding the influence of parameterized model processes, such as convective transport, which shape the vertical distribution of CO concentrations.

Globally, a posteriori anthropogenic CO emissions from Prof-FixOH were slightly lower than those from Col-FixOH, with an average difference of -6.6% over 2003–2022 (Table 2). This difference was more pronounced over North America (-7.9%) and Europe (-7.3%), potentially reflecting weaker convective transport and thus more chemically aged air in the free troposphere over these continents (Jiang et al., 2015a). Eastern China exhibited a unique dynamic evolution (Fig. 3c): a posteriori CO emissions from Prof-FixOH were lower than those from Col-FixOH during 2003-2015 but gradually exceeded them after 2016, reaching a difference of approximately 7% by 2022 (Table S1). Similarly, global biomass burning CO emissions from Prof-FixOH were slightly lower (-5.5% on average) than those from Col-FixOH (Table 2). However, the response of inferred biomass burning emissions to satellite retrievals showed more complex regional discrepancies (Table 3): Prof-FixOH estimates were lower than Col-FixOH in Africa (-11.2%) and Australia (-9.2%) but higher in other regions, particularly Southeast Asia (9.7%).

https://doi.org/10.5194/egusphere-2025-5432
Preprint. Discussion started: 18 November 2025

Furthermore, we found broadly consistent trends in inferred anthropogenic CO emissions between two configurations over 2003-2022. Both Prof-FixOH and Col-FixOH suggest a decrease in global anthropogenic CO emissions of approximately -0.9% yr^{-1}, with slightly larger regional discrepancies for eastern China (-2.1% yr^{-1} and -1.6% yr^{-1}, respectively) and India (1.1% yr^{-1} and 0.7% yr^{-1}, respectively). Similarly, trends in global biomass burning CO emissions were consistent (0.3% yr^{-1} for Col-FixOH and 0.5% yr^{-1} for Prof-FixOH), though regional discrepancies were slightly larger for boreal North America (3.1% yr^{-1} and 4.9% yr^{-1}) and Australia (-1.5% yr^{-1} and -0.7% yr^{-1}). The limited differences in inferred emissions between the two configurations led to consistent declining trends in simulated CO columns (-0.5% yr^{-1} for both). The generally small differences in emission magnitudes and trends inferred from column versus profile retrievals demonstrate the robustness of our central finding, a significant long-term decline in global anthropogenic CO emissions. The regional discrepancies, particularly the evolving difference over eastern China, invite further investigation into potential changes in atmospheric stability or pollution source characteristics differentially constrained by the retrieval types.

3.3.2 Impacts of CO sinks (OH concentrations)

OH concentrations in model simulations significantly influence the inverse analysis of CO emissions (Jiang et al., 2011; Müller et al., 2018). By assimilating MOPITT CO column data, we compared the inverted CO emission estimates driven by fixed (Col-FixOH) and variable (Col-VarOH) OH fields to investigate the potential influence of uncertainties in CO sinks. As shown in Fig. 6c, OH concentrations from the TCR-2 reanalysis are broadly 10-40% lower than the fixed climatological OH concentrations over land (differences over the ocean are not considered here due to the use of CO land boundary conditions in the 4D-Var assimilation). Lower OH concentrations over land lead to reduced chemical loss, which is compensated by lower CO emissions in the Col-VarOH inversion to maintain atmospheric chemical equilibrium

https://doi.org/10.5194/egusphere-2025-5432
Preprint. Discussion started: 18 November 2025

between CO sources and sinks (Fig. 6f). From 2003 to 2022, global anthropogenic emissions in Col-VarOH averaged 590.1 Tg yr^{-1} (Table 2), approximately 3.7% lower than in Col-FixOH (612.8 Tg yr^{-1}). Similarly, a posteriori CO emissions in Col-VarOH were approximately 5.5%, 4.6%, and 7.6% lower than those in Col-FixOH over the US, East China, and India, respectively.

Furthermore, both inversion configurations captured similar temporal evolution in emission changes, including key turning points (e.g., the peak in eastern China's emissions in 2007 and trough in 2008, Fig. 5c) and extreme events (e.g., the biomass burning emission peak in 2021, Fig. 5g). From 2003 to 2022, both configurations suggest consistent trends in global anthropogenic CO emissions (-0.9% yr^{-1}). Regional trends were also similar: -3.5% yr^{-1} and -3.4% yr^{-1} (US), -1.6% yr^{-1} and -2.0% yr^{-1} (eastern China), and 0.7% yr^{-1} and 1.1% yr^{-1} (India) for Col-FixOH and Col-VarOH, respectively. The limited discrepancies in the magnitude and trends of a posteriori CO emissions driven by different OH fields suggest that the impact of uncertainties in CO sinks on our derived emission estimates is minor. This insensitivity can be partially attributed to the use of optimized land boundary CO conditions, which, as indicated by Jiang et al. (2015b), can reduce the impact of OH concentration uncertainties by approximately 50%.

3.3.3 Synthesis and Robustness Assessment

The sensitivity experiments described above collectively address the third objective of this study, which is to evaluate the robustness of our central findings against potential systematic errors associated with satellite retrieval vertical sensitivity and OH concentrations. The comparison between emissions constrained by MOPITT column (Col-FixOH) and profile (Prof-FixOH) data revealed limited discrepancies in both the magnitude and, crucially, the long-term trends of global and regional CO emissions (Section 3.2.1). Similarly, employing variable OH fields (Col-VarOH) instead of a fixed climatology led to only modest differences in the derived emission estimates, without altering the key temporal evolution characteristics

https://doi.org/10.5194/egusphere-2025-5432
Preprint. Discussion started: 18 November 2025

(Section 3.2.2). This robustness can be attributed, in part, to our two-step inversion framework, which mitigates systematic biases through optimized initial and boundary CO conditions. Therefore, we conclude that uncertainties in MOPITT vertical sensitivity and modeled OH fields do not significantly undermine the primary emission trends quantified in this study, thereby increasing confidence in our assessment of the long-term evolution of global CO emissions.

3.4 Long-term evolution and drivers of global CO concentrations

Building on the emission estimates evaluated above, this section investigates their ultimate influence in the atmosphere by analyzing the spatiotemporal patterns and trends of CO concentrations. We first present the mean state and long-term changes in CO concentrations, and then quantitatively attribute these changes to their underlying drivers: emissions and meteorology. Figs. 7a-c show the mean surface CO concentrations in 2003-2022 from the a posteriori simulations and WDCGG surface observations. Higher CO concentrations are evident in regions with strong anthropogenic emissions, such as East Asia, India, and Southeast Asia, as well as in areas with significant biomass burning, i.e., Central Africa and South America. The long-term trends in surface CO (Figs. 7d-f) reveal declining concentrations over North America, Europe, East Asia, and South America, which contrast with rising trends over India, Boreal Asia, Central Africa, and Australia. The 20-year mean CO columns (Figs. 8a-c) show a consistent spatial pattern, with the highest column concentrations over East Asia and Central Africa, followed by South America, India, and Southeast Asia. In contrast, the long-term trend of CO columns (Figs. 8d-f) exhibits a more uniform decrease across the Northern Hemisphere, lacking the distinct regional hotspots observed in the surface trends. This suggests that changes in CO are more thoroughly mixed within the column.

To quantitatively attribute the concentration trends to specific drivers, we conducted a

https://doi.org/10.5194/egusphere-2025-5432
Preprint. Discussion started: 18 November 2025

series of sensitivity experiments. The results indicate that meteorological influences induced positive trends in surface CO concentrations in regions such as central Africa, Southeast Asia, and the Tibetan Plateau (0.6-1.8% yr^{-1}), along with slight negative trends in areas such as South America. The meteorological impact on CO column concentrations was comparatively weaker (Fig. 9b), showing positive trends of 0.45% yr^{-1} over central Africa and the Tibetan Plateau. This vertical differentiation implies that meteorological influences may primarily alter the vertical distribution of CO through changes in convective transport, with a more limited effect on larger horizontal scales. The derived meteorological impact is noticeably weaker than that reported by Jiang et al. (2017), a discrepancy likely attributable to our use of consistent MERRA-2 meteorological fields, which enhances the reliability of the long-term trend analysis. Similarly, the impact of biogenic VOC changes on CO concentrations (Figs. 9g, 9h) was markedly weaker than in Jiang et al. (2017).

Anthropogenic emission changes were identified as the principal driver behind declining CO levels, inducing strong negative trends in industrial regions of the Northern Hemisphere, such as eastern North America, Europe, and eastern China. This signal is consistent across both surface and column concentrations. Globally, anthropogenic emission changes led to an average annual decrease of 0.27% yr^{-1} in CO column concentrations, with a more pronounced decline rate of 0.51% yr^{-1} in the Northern Hemisphere. Regionally, the US, Europe, and eastern China exhibited the most substantial decreases, at -0.57% yr^{-1}, -0.69% yr^{-1} and -0.69% yr^{-1}, respectively. In contrast, India experienced a slight concentration increase (0.03% yr^{-1}) due to rising emissions, while Southeast Asia showed a more moderate decline (-0.19% yr^{-1}) compared to other major industrial regions.

Conversely, changes in biomass burning emissions generally contributed to positive CO trends, particularly in high-latitude regions. Globally, biomass burning emissions led to an average annual increase of 0.10% yr^{-1} in CO column concentrations, with a more significant

https://doi.org/10.5194/egusphere-2025-5432
Preprint. Discussion started: 18 November 2025

rise of 0.24% yr^{-1} in the Northern Hemisphere. Notable increases occurred in Boreal North America (0.43% yr^{-1}) and Boreal Asia (0.48% yr^{-1}), whereas South America, Australia, and Southeast Asia experienced declining trends ranging from -0.13% yr^{-1} to -0.22 yr^{-1}; Africa exhibited a slight increase of 0.09% yr^{-1}.

This attribution analysis quantitatively confirms a substantial offsetting effect from biomass burning emissions. Although anthropogenic emission reductions lowered Northern Hemisphere CO column concentrations by approximately 0.51% yr^{-1}, the concomitant rise in biomass burning emissions counteracted this trend by adding about 0.24% yr^{-1}. As a result, the net concentration decline was limited to approximately 0.27% yr^{-1}, indicating that nearly half (47%) of the potential air quality improvement from anthropogenic emission controls has been offset by the intensification of fires. This finding provides a clear mechanistic explanation for the attenuated decline in atmospheric CO concentrations in recent years, establishing a direct link to climate-change-amplified wildfire activity.

4. Conclusions

This study provides an updated, quantitative analysis of global CO emissions and drivers of atmospheric CO trends from 2003 to 2022, using an extended GEOS-Chem adjoint model constrained by MOPITT satellite observations. A key methodological advancement was the use of continuous MERRA-2 meteorological data and updated a priori emission inventories, which improved the long-term consistency and convergence efficiency of the 4D-Var assimilation system. The implementation of a two-step bias mitigation strategy, optimizing both initial conditions and land boundary conditions for CO, effectively reduced the accumulated impacts of transport and chemistry uncertainties, lending to weaker sensitivity to uncertainties in satellite vertical sensitivity and OH concentrations.

The optimized a posteriori emission estimates were rigorously evaluated against independent surface (WDCGG) and aircraft (ATOM, HIPPO) observations. This evaluation

https://doi.org/10.5194/egusphere-2025-5432
Preprint. Discussion started: 18 November 2025

demonstrated a noticeable improvement in model performance. The mean bias in simulated CO concentrations was reduced from -3.8 ppb in the a priori simulation to between -2.5 and -2.1 ppb in the a posteriori simulation for HIPPO, and from -3.4 ppb in the a priori simulation to between -2.9 and -1.6 ppb in the a posteriori simulation for ATOM. Similarly, biases against surface observations were reduced, confirming the robustness of the inversion results. Consistent with previous studies focusing on shorter periods, our two-decade analysis reveals a pronounced decline of 14-17% in global anthropogenic CO emissions, equivalent to a reduction of approximately 85-110 Tg. This decline was primarily driven by emission reduction efforts in major industrialized regions, with cumulative reductions estimated at 46–49% in the US, 32–34% in Europe, and 23–32% in eastern China. In contrast, biomass burning emissions exhibited strong interannual variability, with a notable recent increase in Northern Hemisphere high-latitude forests.

A critical finding of this work is the substantial offsetting effect of increasing biomass burning emissions on atmospheric CO levels. Our attribution analysis shows that while anthropogenic emission reductions decreased the Northern Hemisphere CO column concentration at a rate of approximately 0.51% yr^{-1}, concurrent increases in biomass burning emissions counteracted this trend by adding about 0.24% yr^{-1}. The net decline was therefore limited to only 0.27% yr^{-1}, indicating that nearly half (47%) of the potential air quality improvement from anthropogenic emission controls was offset by enhanced biomass burning. This substantial offsetting effect implies that the carbon mitigation benefits achieved by reducing fossil fuel combustion are being concurrently attenuated by climate-driven carbon releases from wildfires. Our analysis thus not only clarifies the past evolution of global CO emissions and concentrations but also highlights an increasingly critical challenge: climate change is actively undermining emission control efforts by intensifying natural fire activities, underscoring the need for integrated policies that address both anthropogenic sources and the

https://doi.org/10.5194/egusphere-2025-5432
Preprint. Discussion started: 18 November 2025

climate-driven amplification of natural emissions.

Code and data availability: The MOPITT CO data can be downloaded from https://asdc.larc.nasa.gov/data/MOPITT/. The adjoint of GEOS-Chem model can be downloaded from http://wiki.seas.harvard.edu/geos-chem/index.php/GEOS-Chem_Adjoint. The a posteriori CO emission estimates (Col-FixOH, Prof-FixOH and Col-VarOH) can be downloaded from https://doi.org/10.5281/zenodo.17221834.

Author Contributions: Z.J. designed the research. Z.T. developed the model code and performed the research. Z.J. and Z.T. wrote the manuscript. All authors contributed to discussions and editing the manuscript.

Competing interests: The authors declare that they have no conflicts of interest.

Acknowledgments: We thank the providers of the MOPITT CO data. The numerical calculations in this paper have been done on the supercomputing system in the Supercomputing Center of University of Science and Technology of China. This work was supported by the National Natural Science Foundation of China (42277082). Part of this work was conducted at the Jet Propulsion Laboratory, California Institute of Technology, under contract with NASA.

Tables and Figures

Table 1. Mean biases of modeled CO concentrations relative to satellite and in-situ observations for five model configurations. Configurations include GC-original (using original monthly CO initial conditions + a priori emission inventories), GC-a priori (using optimized monthly CO initial conditions + a priori emission inventories), and three a posteriori simulations (using optimized initial conditions + optimized emission inventories). Biases are presented in units of 10^{16} molecules cm^{-2} for MOPITT and ppb for other datasets.

https://doi.org/10.5194/egusphere-2025-5432
Preprint. Discussion started: 18 November 2025

Table 2. Mean anthropogenic CO emissions (Tg yr^{-1}) and their trends in 2003-2022 in the a priori inventories and those constrained by MOPITT column (Col) and profile (Prof) retrievals with fixed (Fix) and variable (Var) OH fields. The region definition is shown in Figure S1e.

Table 3. Mean biomass burning CO emissions (Tg yr^{-1}) and their trends in 2003-2022 in the a priori inventories and those constrained by MOPITT column (Col) and profile (Prof) retrievals with fixed (Fix) and variable (Var) OH fields. The region definition is shown in Figure S1f.

Table 4. Trends in column CO concentrations (% yr^{-1}) driven by changes in anthropogenic and biomass burning emissions (based on Col-FixOH in 2003-2022). Values represent the annual percentage change in CO columns due solely to changes in one type of sources.

Fig. 1. (a-c) Mean a priori CO emissions from 2003 to 2022 with unit 10^{12} molecules cm^{-2} s^{-1}; (d-f) Scaling factors of Col-FixOH; (g-i) Scaling factors of Prof-FixOH; (j-l) Scaling factors of Col-VarOH. The scaling factors are the ratios between a posteriori to a priori CO emissions.

Fig. 2. Relative bias in column CO for 2003-2022, calculated as (Model - MOPITT) / MOPITT for GC-original (a), GC-a priori (b), and the a posteriori simulations (c-e).

Fig. 3. Twelve-month moving average of anthropogenic CO emissions (Tg $month^{-1}$) in 2003-2022. The series includes the a priori emission (green) and the a posteriori emissions constrained with Col-FixOH (blue), Prof-FixOH (magenta) and Col-VarOH (red). The region definition is shown in Figure S1e.

Fig. 4. Trends in CO emissions (10^{10} molecules cm^{-2} s^{-1} yr^{-1}) from 2003 to 2022, as constrained by different MOPITT data sets and OH configurations. Months where biomass burning CO emissions contributed >50% of the total emissions in a grid cell were excluded from the trend calculations for anthropogenic and biogenic VOC emissions.

Fig. 5. Monthly biomass burning CO emissions (with unit Tg $month^{-1}$) in 2003-2022: a priori emission (green) and a posteriori emissions constrained with Col-FixOH (blue), Prof-FixOH (magenta) and Col-VarOH (red). The region definition is shown in Figure S1f.

https://doi.org/10.5194/egusphere-2025-5432
Preprint. Discussion started: 18 November 2025

Fig. 6. Comparison of OH fields and their impact on emission estimates. (a-c) Tropospheric OH columns (10^{12} molecules cm^{-2}) averaged over 2003-2022 from (a) the fixed OH field, (b) the variable OH field, and (c) their difference (Variable - Fixed). (d-f) The corresponding CO emission scaling factors from (d) the Col-FixOH inversion, (e) the Col-VarOH inversion, and (f) the difference between them (Col-VarOH - Col-FixOH).

Fig. 7. (a-c) Mean surface CO concentrations (ppb) for 2003-2022 from WDCGG observations and model simulations. (d-f) Trend of surface CO concentration from observations and model simulations. Only stations with 20 year observations (the time range between the first and last observations) during 2003-2022 are included.

Fig. 8. (a-c) Mean modeled column CO concentrations (10^{18} molecules cm^{-2}) from 2003 to 2022. (d-f) Trend of modeled column CO concentrations (% yr^{-1}) from 2003 to 2022.

Fig. 9. Attribution of trends (% yr^{-1}) in surface and column CO from 2003 to 2022 to specific emission sectors, based on sensitivity simulations. Trends are shown for scenarios with: (a, b) all emissions fixed at 2003 levels; (c, d) only anthropogenic emissions varying over time; (e, f) only biomass burning emissions varying; (g, h) only biogenic VOC emissions varying. The varying emissions in these scenarios are prescribed from the Col-FixOH a posteriori inversion.

References

Andela, N., Morton, D. C., Giglio, L., Chen, Y., van der Werf, G. R., Kasibhatla, P. S., DeFries, R. S., Collatz, G. J., Hantson, S., Kloster, S., Bachelet, D., Forrest, M., Lasslop, G., Li, F., Mangeon, S., Melton, J. R., Yue, C., and Randerson, J. T.: A human-driven decline in global burned area, Science, 356, 1356-1362, 10.1126/science.aal4108, 2017.

Arellano, A. F., Kasibhatla, P. S., Giglio, L., van der Werf, G. R., and Randerson, J. T.: Top-down estimates of global CO sources using MOPITT measurements, Geophys. Res. Lett., 31, L01104, 10.1029/2003gl018609, 2004.

Bloom, A. A., Worden, J., Jiang, Z., Worden, H., Kurosu, T., Frankenberg, C., and Schimel, D.: Remote-sensing constraints on South America fire traits by Bayesian fusion of atmospheric and surface data, Geophys. Res. Lett., 42, 1268-1274, 10.1002/2014gl062584, 2015.

Buchholz, R. R., Park, M., Worden, H. M., Tang, W., Edwards, D. P., Gaubert, B., Deeter, M. N., Sullivan, T., Ru, M., Chin, M., Levy, R. C., Zheng, B., and Magzamen, S.: New seasonal pattern of pollution emerges from changing North American wildfires, Nat. Commun., 13, 2043, 10.1038/s41467-022-29623-8, 2022.

https://doi.org/10.5194/egusphere-2025-5432
Preprint. Discussion started: 18 November 2025

Deb, P., Moradkhani, H., Abbaszadeh, P., Kiem, A. S., Engström, J., Keellings, D., and Sharma, A.: Causes of the Widespread 2019–2020 Australian Bushfire Season, Earth's Future, 8, e2020EF001671, 10.1029/2020ef001671, 2020.

Deeter, M., Francis, G., Gille, J., Mao, D., Martínez-Alonso, S., Worden, H., Ziskin, D., Drummond, J., Commane, R., Diskin, G., and McKain, K.: The MOPITT Version 9 CO product: sampling enhancements and validation, Atmos. Meas. Tech., 15, 2325-2344, 10.5194/amt-15-2325-2022, 2022.

Elguindi, N., Granier, C., Stavrakou, T., Darras, S., Bauwens, M., Cao, H., Chen, C., Denier van der Gon, H. A. C., Dubovik, O., Fu, T. M., Henze, D. K., Jiang, Z., Keita, S., Kuenen, J. J. P., Kurokawa, J., Liousse, C., Miyazaki, K., Müller, J. F., Qu, Z., Solmon, F., and Zheng, B.: Intercomparison of Magnitudes and Trends in Anthropogenic Surface Emissions From Bottom‐Up Inventories, Top‐Down Estimates, and Emission Scenarios, Earth's Future, 8, e2020EF001520, 10.1029/2020ef001520, 2020.

Field, R. D., van der Werf, G. R., Fanin, T., Fetzer, E. J., Fuller, R., Jethva, H., Levy, R., Livesey, N. J., Luo, M., Torres, O., and Worden, H. M.: Indonesian fire activity and smoke pollution in 2015 show persistent nonlinear sensitivity to El Nino-induced drought, Proc. Natl. Acad. Sci. USA, 113, 9204-9209, 10.1073/pnas.1524888113, 2016.

Fisher, J. A., Murray, L. T., Jones, D. B. A., and Deutscher, N. M.: Improved method for linear carbon monoxide simulation and source attribution in atmospheric chemistry models illustrated using GEOS-Chem v9, Geosci. Model Dev., 10, 4129-4144, 10.5194/gmd-10-4129-2017, 2017.

Fortems-Cheiney, A., Chevallier, F., Pison, I., Bousquet, P., Szopa, S., Deeter, M. N., and Clerbaux, C.: Ten years of CO emissions as seen from Measurements of Pollution in the Troposphere (MOPITT), J. Geophys. Res.-Atmos., 116, D05304, 10.1029/2010jd014416, 2011.

Fortems-Cheiney, A., Broquet, G., Potier, E., Plauchu, R., Berchet, A., Pison, I., Denier van der Gon, H., and Dellaert, S.: CO anthropogenic emissions in Europe from 2011 to 2021: insights from Measurement of Pollution in the Troposphere (MOPITT) satellite data, Atmos. Chem. Phys., 24, 4635-4649, 10.5194/acp-24-4635-2024, 2024.

Guenther, A., Karl, T., Harley, P., Wiedinmyer, C., Palmer, P. I., and Geron, C.: Estimates of global terrestrial isoprene emissions using MEGAN (Model of Emissions of Gases and Aerosols from Nature), Atmos. Chem. Phys., 6, 3181-3210, 10.5194/acp-6-3181-2006, 2006.

Heald, C. L., Jacob, D. J., Jones, D. B. A., Palmer, P. I., Logan, J. A., Streets, D. G., Sachse, G. W., Gille, J. C., Hoffman, R. N., and Nehrkorn, T.: Comparative inverse analysis of satellite (MOPITT) and aircraft (TRACE-P) observations to estimate Asian sources of carbon monoxide, J. Geophys. Res.-Atmos., 109, D23306, 10.1029/2004jd005185, 2004.

Hedelius, J. K., Toon, G. C., Buchholz, R. R., Iraci, L. T., Podolske, J. R., Roehl, C. M., Wennberg, P. O., Worden, H. M., and Wunch, D.: Regional and urban column CO trends and anomalies as observed by MOPITT over 16 years, J. Geophys. Res.-Atmos., 126, e2020JD033967, 10.1029/2020jd033967, 2021.

Henze, D. K., Hakami, A., and Seinfeld, J. H.: Development of the adjoint of GEOS-Chem, Atmos. Chem. Phys., 7, 2413-2433, 10.5194/acp-7-2413-2007, 2007.

https://doi.org/10.5194/egusphere-2025-5432
Preprint. Discussion started: 18 November 2025

Hoesly, R. M., Smith, S. J., Feng, L., Klimont, Z., Janssens-Maenhout, G., Pitkanen, T., Seibert, J. J., Vu, L., Andres, R. J., Bolt, R. M., Bond, T. C., Dawidowski, L., Kholod, N., Kurokawa, J.-i., Li, M., Liu, L., Lu, Z., Moura, M. C. P., O'Rourke, P. R., and Zhang, Q.: Historical (1750–2014) anthropogenic emissions of reactive gases and aerosols from the Community Emissions Data System (CEDS), Geosci. Model Dev., 11, 369-408, 10.5194/gmd-11-369-2018, 2018.

Hooghiemstra, P. B., Krol, M. C., van Leeuwen, T. T., van der Werf, G. R., Novelli, P. C., Deeter, M. N., Aben, I., and Röckmann, T.: Interannual variability of carbon monoxide emission estimates over South America from 2006 to 2010, J. Geophys. Res.-Atmos., 117, D15308, 10.1029/2012jd017758, 2012.

Hu, W., Zhao, Y., Lu, N., Wang, X., Zheng, B., Henze, D. K., Zhang, L., Fu, T. M., and Zhai, S.: Changing Responses of $PM_{2.5}$ and Ozone to Source Emissions in the Yangtze River Delta Using the Adjoint Model, Environ. Sci. Technol., 58, 628-638, 10.1021/acs.est.3c05049, 2024.

Huijnen, V., Wooster, M. J., Kaiser, J. W., Gaveau, D. L., Flemming, J., Parrington, M., Inness, A., Murdiyarso, D., Main, B., and van Weele, M.: Fire carbon emissions over maritime southeast Asia in 2015 largest since 1997, Sci. Rep., 6, 26886, 10.1038/srep26886, 2016.

Jain, P., Barber, Q. E., Taylor, S. W., Whitman, E., Castellanos Acuna, D., Boulanger, Y., Chavardès, R. D., Chen, J., Englefield, P., Flannigan, M., Girardin, M. P., Hanes, C. C., Little, J., Morrison, K., Skakun, R. S., Thompson, D. K., Wang, X., and Parisien, M.-A.: Drivers and Impacts of the Record-Breaking 2023 Wildfire Season in Canada, Nat. Commun., 15, 6764, 10.1038/s41467-024-51154-7, 2024.

Jiang, Z., Jones, D. B. A., Kopacz, M., Liu, J., Henze, D. K., and Heald, C.: Quantifying the impact of model errors on top-down estimates of carbon monoxide emissions using satellite observations, J. Geophys. Res.-Atmos., 116, D15306, 10.1029/2010jd015282, 2011.

Jiang, Z., Jones, D. B. A., Worden, H. M., and Henze, D. K.: Sensitivity of top-down CO source estimates to the modeled vertical structure in atmospheric CO, Atmos. Chem. Phys., 15, 1521-1537, 10.5194/acp-15-1521-2015, 2015a.

Jiang, Z., Jones, D. B. A., Worden, J., Worden, H. M., Henze, D. K., and Wang, Y. X.: Regional data assimilation of multi-spectral MOPITT observations of CO over North America, Atmos. Chem. Phys., 15, 6801-6814, 10.5194/acp-15-6801-2015, 2015b.

Jiang, Z., Worden, J. R., Worden, H., Deeter, M., Jones, D. B. A., Arellano, A. F., and Henze, D. K.: A 15-year record of CO emissions constrained by MOPITT CO observations, Atmos. Chem. Phys., 17, 4565-4583, 10.5194/acp-17-4565-2017, 2017.

Jiang, Z., Lin, J., He, T.-L., Jiang, F., Jin, J., Qin, K., Shen, L., Yang, P., Zang, Z., Zhang, L., Zhang, Y., Zheng, B., Zhong, H., and Zhu, L.: Satellite-Based Emission Inversion for Air Pollutants and Greenhouse Gases: A Review, J. Meteor. Res., 39, 1101-1125, 10.1007/s13351-025-4914-7, 2025.

Jolly, W. M., Cochrane, M. A., Freeborn, P. H., Holden, Z. A., Brown, T. J., Williamson, G. J., and Bowman, D. M.: Climate-induced variations in global wildfire danger from 1979 to 2013, Nat. Commun., 6, 7537, 10.1038/ncomms8537, 2015.

https://doi.org/10.5194/egusphere-2025-5432
Preprint. Discussion started: 18 November 2025

Jones, M. W., Veraverbeke, S., Andela, N., Doerr, S. H., Kolden, C., Mataveli, G., Pettinari, M. L., Le Quere, C., Rosan, T. M., van der Werf, G. R., van Wees, D., and Abatzoglou, J. T.: Global rise in forest fire emissions linked to climate change in the extratropics, Science, 386, eadl5889, 10.1126/science.adl5889, 2024.

Justino, F., Bromwich, D., Wilson, A., Silva, A., Avila-Diaz, A., Fernandez, A., and Rodrigues, J.: Estimates of temporal-spatial variability of wildfire danger across the Pan-Arctic and extra-tropics, Environ. Res. Let., 16, 044060, 10.1088/1748-9326/abf0d0, 2021.

Keller, C. A., Long, M. S., Yantosca, R. M., Da Silva, A. M., Pawson, S., and Jacob, D. J.: HEMCO v1.0: a versatile, ESMF-compliant component for calculating emissions in atmospheric models, Geosci. Model Dev., 7, 1409-1417, 10.5194/gmd-7-1409-2014, 2014.

Kopacz, M., Jacob, D. J., Fisher, J. A., Logan, J. A., Zhang, L., Megretskaia, I. A., Yantosca, R. M., Singh, K., Henze, D. K., Burrows, J. P., Buchwitz, M., Khlystova, I., McMillan, W. W., Gille, J. C., Edwards, D. P., Eldering, A., Thouret, V., and Nedelec, P.: Global estimates of CO sources with high resolution by adjoint inversion of multiple satellite datasets (MOPITT, AIRS, SCIAMACHY, TES), Atmos. Chem. Phys., 10, 855-876, 10.5194/acp-10-855-2010, 2010.

Kurokawa, J., and Ohara, T.: Long-term historical trends in air pollutant emissions in Asia: Regional Emission inventory in ASia (REAS) version 3, Atmos. Chem. Phys., 20, 12761-12793, 10.5194/acp-20-12761-2020, 2020.

Li, M., Zhang, Q., Kurokawa, J.-i., Woo, J.-H., He, K., Lu, Z., Ohara, T., Song, Y., Streets, D. G., Carmichael, G. R., Cheng, Y., Hong, C., Huo, H., Jiang, X., Kang, S., Liu, F., Su, H., and Zheng, B.: MIX: a mosaic Asian anthropogenic emission inventory under the international collaboration framework of the MICS-Asia and HTAP, Atmos. Chem. Phys., 17, 935-963, 10.5194/acp-17-935-2017, 2017.

Lin, H., Jacob, D. J., Lundgren, E. W., Sulprizio, M. P., Keller, C. A., Fritz, T. M., Eastham, S. D., Emmons, L. K., Campbell, P. C., Baker, B., Saylor, R. D., and Montuoro, R.: Harmonized Emissions Component (HEMCO) 3.0 as a versatile emissions component for atmospheric models: application in the GEOS-Chem, NASA GEOS, WRF-GC, CESM2, NOAA GEFS-Aerosol, and NOAA UFS models, Geosci. Model Dev., 14, 5487-5506, 10.5194/gmd-14-5487-2021, 2021.

Lin, J. T., and McElroy, M. B.: Detection from space of a reduction in anthropogenic emissions of nitrogen oxides during the Chinese economic downturn, Atmos. Chem. Phys., 11, 8171-8188, 10.5194/acp-11-8171-2011, 2011.

Messina, P., Lathière, J., Sindelarova, K., Vuichard, N., Granier, C., Ghattas, J., Cozic, A., and Hauglustaine, D. A.: Global biogenic volatile organic compound emissions in the ORCHIDEE and MEGAN models and sensitivity to key parameters, Atmos. Chem. Phys., 16, 14169-14202, 10.5194/acp-16-14169-2016, 2016.

Miyazaki, K., Bowman, K., Sekiya, T., Eskes, H., Boersma, F., Worden, H., Livesey, N., Payne, V. H., Sudo, K., Kanaya, Y., Takigawa, M., and Ogochi, K.: Updated tropospheric chemistry reanalysis and emission estimates, TCR-2, for 2005–2018, Earth Syst. Sci. Data, 12, 2223-2259, 10.5194/essd-12-2223-2020, 2020.

https://doi.org/10.5194/egusphere-2025-5432
Preprint. Discussion started: 18 November 2025

Müller, J. F., Stavrakou, T., Bauwens, M., George, M., Hurtmans, D., Coheur, P. F., Clerbaux, C., and Sweeney, C.: Top‐Down CO Emissions Based On IASI Observations and Hemispheric Constraints on OH Levels, Geophys. Res. Lett., 45, 1621-1629, 10.1002/2017gl076697, 2018.

Page, S., Hoscilo, A., Langner, A., Tansey, K., Siegert, F., Limin, S., and Rieley, J.: Tropical peatland fires in Southeast Asia, in: Tropical Fire Ecology: Climate Change, Land Use, and Ecosystem Dynamics, edited by: Cochrane, M. A., Springer Praxis Books, Springer, Berlin, Heidelberg, 2009.

Qu, Z., Henze, D. K., Worden, H. M., Jiang, Z., Gaubert, B., Theys, N., and Wang, W.: Sector-based top-down estimates of NO_x, SO_2, and CO emissions in East Asia, Geophys. Res. Lett., 49, e2021GL096009, 10.1029/2021gl096009, 2022.

Silva Junior, C. H. L., Pessôa, A. C. M., Carvalho, N. S., Reis, J. B. C., Anderson, L. O., and Aragão, L. E. O. C.: The Brazilian Amazon deforestation rate in 2020 is the greatest of the decade, Nature Ecology & Evolution, 5, 144-145, 2021.

Smoydzin, L., and Hoor, P.: Contribution of Asian emissions to upper tropospheric CO over the remote Pacific, Atmos. Chem. Phys., 22, 7193-7206, 10.5194/acp-22-7193-2022, 2022.

Tan, H., Zhang, L., Lu, X., Zhao, Y., Yao, B., Parker, R. J., and Boesch, H.: An integrated analysis of contemporary methane emissions and concentration trends over China using in situ and satellite observations and model simulations, Atmos. Chem. Phys., 22, 1229-1249, 10.5194/acp-22-1229-2022, 2022.

Tang, W., Arellano, A. F., Gaubert, B., Miyazaki, K., and Worden, H. M.: Satellite data reveal a common combustion emission pathway for major cities in China, Atmos. Chem. Phys., 19, 4269-4288, 10.5194/acp-19-4269-2019, 2019.

Tang, W., Gaubert, B., Emmons, L., Ziskin, D., Mao, D., Edwards, D., Arellano, A., Raeder, K., Anderson, J., and Worden, H.: Advantages of assimilating multispectral satellite retrievals of atmospheric composition: a demonstration using MOPITT carbon monoxide products, Atmos. Meas. Tech., 17, 1941-1963, 10.5194/amt-17-1941-2024, 2024.

Tang, Z., Chen, J., and Jiang, Z.: Discrepancy in assimilated atmospheric CO over East Asia in 2015–2020 by assimilating satellite and surface CO measurements, Atmos. Chem. Phys., 22, 7815-7826, 10.5194/acp-22-7815-2022, 2022.

Tang, Z., Jiang, Z., Chen, J., Yang, P., and Shen, Y.: The capabilities of the adjoint of GEOS-Chem model to support HEMCO emission inventories and MERRA-2 meteorological data, Geosci. Model Dev., 16, 6377-6392, 10.5194/gmd-16-6377-2023, 2023.

Todling, R., and Cohn, S. E.: Suboptimal schemes for atmospheric data assimilation based on the Kalman filter, Monthly Weather Review, 122, 10.1175/1520-0493(1994)122<2530:SSFADA>2.0.CO;2, 1994.

Tong, D., Pan, L., Chen, W., Lamsal, L., Lee, P., Tang, Y., Kim, H., Kondragunta, S., and Stajner, I.: Impact of the 2008 Global Recession on air quality over the United States: Implications for surface ozone levels from changes in NO_x emissions, Geophys. Res. Lett., 43, 9280-9288, 10.1002/2016gl069885, 2016.

van der Werf, G. R., Randerson, J. T., Giglio, L., Collatz, G. J., Mu, M., Kasibhatla, P. S., Morton, D. C., DeFries, R. S., Jin, Y., and van Leeuwen, T. T.: Global fire emissions and the

https://doi.org/10.5194/egusphere-2025-5432
Preprint. Discussion started: 18 November 2025

contribution of deforestation, savanna, forest, agricultural, and peat fires (1997–2009), Atmos. Chem. Phys., 10, 11707-11735, 10.5194/acp-10-11707-2010, 2010.

Wang, H., Lu, X., Jacob, D. J., Cooper, O. R., Chang, K. L., Li, K., Gao, M., Liu, Y., Sheng, B., Wu, K., Wu, T., Zhang, J., Sauvage, B., Nédélec, P., Blot, R., and Fan, S.: Global tropospheric ozone trends, attributions, and radiative impacts in 1995–2017: an integrated analysis using aircraft (IAGOS) observations, ozonesonde, and multi-decadal chemical model simulations, Atmos. Chem. Phys., 22, 13753-13782, 10.5194/acp-22-13753-2022, 2022.

Warner, J., Carminati, F., Wei, Z., Lahoz, W., and Attié, J. L.: Tropospheric carbon monoxide variability from AIRS under clear and cloudy conditions, Atmos. Chem. Phys., 13, 12469-12479, 10.5194/acp-13-12469-2013, 2013.

Whaley, C. H., Strong, K., Jones, D. B. A., Walker, T. W., Jiang, Z., Henze, D. K., Cooke, M. A., McLinden, C. A., Mittermeier, R. L., Pommier, M., and Fogal, P. F.: Toronto area ozone: Long-term measurements and modeled sources of poor air quality events, J. Geophys. Res.-Atmos., 120, 11368-11390, 10.1002/2014JD022984, 2015.

Wofsy, S. C., and HIPPO Science Team: HIAPER Pole-to-Pole Observations (HIPPO): fine-grained, global-scale measurements of climatically important atmospheric gases and aerosols, Philosophical Transactions of the Royal Society A: Mathematical, Physical and Engineering Sciences, 369, 2073-2086, 10.1098/rsta.2010.0313, 2011.

Wofsy, S. C., and Atom Science Team: ATom: Aircraft Flight Track and Navigational Data. ORNL DAAC, Oak Ridge, Tennessee, USA. , 10.3334/ORNLDAAC/1613, 2018.

Worden, H. M., Deeter, M. N., Edwards, D. P., Gille, J. C., Drummond, J. R., and Nédélec, P.: Observations of near-surface carbon monoxide from space using MOPITT multispectral retrievals, J. Geophys. Res.-Atmos., 115, D18314, 10.1029/2010jd014242, 2010.

Worden, H. M., Deeter, M. N., Frankenberg, C., George, M., Nichitiu, F., Worden, J., Aben, I., Bowman, K. W., Clerbaux, C., Coheur, P. F., de Laat, A. T. J., Detweiler, R., Drummond, J. R., Edwards, D. P., Gille, J. C., Hurtmans, D., Luo, M., Martínez-Alonso, S., Massie, S., Pfister, G., and Warner, J. X.: Decadal record of satellite carbon monoxide observations, Atmos. Chem. Phys., 13, 837-850, 10.5194/acp-13-837-2013, 2013.

Worden, J. R., Bloom, A. A., Pandey, S., Jiang, Z., Worden, H. M., Walker, T. W., Houweling, S., and Rockmann, T.: Reduced biomass burning emissions reconcile conflicting estimates of the post-2006 atmospheric methane budget, Nat. Commun., 8, 2227, 10.1038/s41467-017-02246-0, 2017.

Xia, Y., Zhao, Y., and Nielsen, C. P.: Benefits of China's efforts in gaseous pollutant control indicated by the bottom-up emissions and satellite observations 2000–2014, Atmos. Environ., 136, 43-53, 10.1016/j.atmosenv.2016.04.013, 2016.

Zhao, Y., Nielsen, C. P., McElroy, M. B., Zhang, L., and Zhang, J.: CO emissions in China: Uncertainties and implications of improved energy efficiency and emission control, Atmos. Environ., 49, 103-113, 10.1016/j.atmosenv.2011.12.015, 2012.

Zhao, Y., Saunois, M., Bousquet, P., Lin, X., Berchet, A., Hegglin, M. I., Canadell, J. G., Jackson, R. B., Deushi, M., Jöckel, P., Kinnison, D., Kirner, O., Strode, S., Tilmes, S., Dlugokencky, E. J., and Zheng, B.: On the role of trend and variability in the hydroxyl radical

https://doi.org/10.5194/egusphere-2025-5432
Preprint. Discussion started: 18 November 2025

(OH) in the global methane budget, Atmos. Chem. Phys., 20, 13011-13022, 10.5194/acp-20-13011-2020, 2020.

Zheng, B., Chevallier, F., Ciais, P., Yin, Y., Deeter, M. N., Worden, H. M., Wang, Y., Zhang, Q., and He, K.: Rapid decline in carbon monoxide emissions and export from East Asia between years 2005 and 2016, Environ. Res. Let., 13, 044007, 10.1088/1748-9326/aab2b3, 2018.

Zheng, B., Ciais, P., Chevallier, F., Chuvieco, E., Chen, Y., and Yang, H.: Increasing forest fire emissions despite the decline in global burned area, Sci. Adv., 7, eabh2646, 10.1126/sciadv.abh2646, 2021.

Zheng, B., Ciais, P., Chevallier, F., Yang, H., Canadell, J. G., Chen, Y., van der Velde, I. R., Aben, I., Chuvieco, E., Davis, S. J., Deeter, M., Hong, C., Kong, Y., Li, H., Li, H., Lin, X., He, K., and Zhang, Q.: Record-high CO_2 emissions from boreal fires in 2021, Science, 379, 912-917, 10.1126/science.ade0805, 2023.

Zhu, C., Byrd, R. H., Lu, P., and Nocedal, J.: Algorithm 778: L-BFGS-B: Fortran Subroutines for Large-Scale Bound Constrained Optimization, ACM Transactions on Mathematical Software, 23, 550-560, 10.1145/279232.279236, 1997.

https://doi.org/10.5194/egusphere-2025-5432
Preprint. Discussion started: 18 November 2025

Observations	GC-original	GC-a priori	Col-FixOH	Prof-FixOH	Col-VarOH
MOPITT	-39.4	-9.7	-7.3	-6.8	-5.1
WDGCC	-20.1	-2.4	1.8	1.7	0.4
HIPPO	-18.9	-3.8	-2.5	-2.1	-2.2
ATOM	-16.2	-3.4	-2.1	-2.9	-1.6

Table 1. Mean biases of modeled CO concentrations relative to satellite and in-situ observations for five model configurations. Configurations include GC-original (using original monthly CO initial conditions + a priori emission inventories), GC-a priori (using optimized monthly CO initial conditions + a priori emission inventories), and three a posteriori simulations (using optimized initial conditions + optimized emission inventories). Biases are presented in units of 10^{16} molecules cm^{-2} for MOPITT and ppb for other datasets.

Anthropogenic emissions		US	Europe	E. China	India	SE. Asia	Global
GC-a priori	Emissions	53.5	33.7	179.6	72.7	26.1	536.3
	Trends	-1.8 ± 0.1	-0.7 ± 0.1	-1.4 ± 0.3	0.3 ± 0.1	0.1 ± 0.0	-3.6 ± 0.4
Col-FixOH	Emissions	61.6	39.2	195.8	73.3	26.9	612.8
	Trends	-2.2 ± 0.3	−0.9 ± 0.2	−4.0 ± 0.8	0.8 ± 0.3	0.0 ± 0.1	−5.6 ± 0.9
Prof-FixOH	Emissions	56.7	36.3	188.3	69.9	26.8	572.2
	Trends	−2.0 ± 0.3	−0.8 ± 0.2	−3.0 ± 0.4	0.5 ± 0.2	0.1 ± 0.1	−5.0 ± 0.4
Col-VarOH	Emissions	58.2	38.5	186.7	67.7	26.3	590.1
	Trends	−2.0 ± 0.3	−0.9 ± 0.2	−3.7 ± 0.8	0.7 ± 0.2	−0.0 ± 0.1	−5.3 ± 0.8

Table 2. Mean anthropogenic CO emissions (Tg yr^{-1}) and their trends in 2003-2022 in the a priori inventories and those constrained by MOPITT column (Col) and profile (Prof) retrievals with fixed (Fix) and variable (Var) OH fields. The region definition is shown in Figure S1e.

Biomass burning	Boreal N. America	Boreal Asia	S. America	Africa	SE. Asia	Australia	Global
GC-a priori	21.50	39.50	44.00	136.90	25.00	12.00	312.50
Col-FixOH	20.41	45.38	37.42	167.51	17.99	15.08	345.61
Prof-FixOH	21.24	46.68	38.37	148.76	19.73	13.70	326.56
Col-VarOH	18.03	41.02	33.30	159.48	18.98	15.81	325.75

Table 3. Mean biomass burning CO emissions (Tg yr^{-1}) and their trends in 2003-2022 in the a priori inventories and those constrained by MOPITT column (Col) and profile (Prof) retrievals with fixed (Fix) and variable (Var) OH fields. The region definition is shown in Figure S1f.

https://doi.org/10.5194/egusphere-2025-5432
Preprint. Discussion started: 18 November 2025

Region	Anthropogenic	Region	Biomass burning
United States	-0.57%	Boreal N. America	0.43%
Europe	-0.69%	Boreal Asia	0.48%
Eastern China	-0.69%	South America	-0.13%
India	0.03%	Africa	0.09%
Southeast Asia	-0.19%	Southeast Asia	-0.22%
\	\	Australia	-0.12%
Northern Hemisphere	-0.51%	Northern Hemisphere	0.24%
Global	-0.27%	Global	0.10%

Table 4. Trends in column CO concentrations (% yr^{-1}) driven by changes in anthropogenic and biomass burning emissions (based on Col-FixOH in 2003-2022). Values represent the annual percentage change in CO columns due solely to changes in one type of sources.

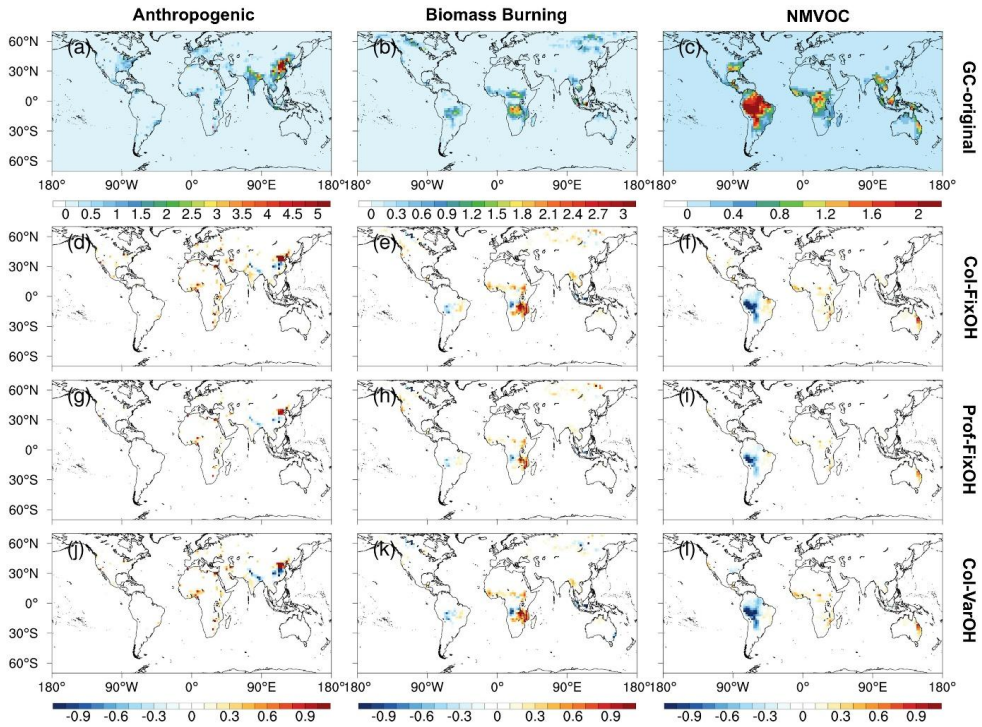

Fig. 1. (a-c) Mean a priori CO emissions from 2003 to 2022 with unit 10^{12} molecules cm^{-2} s^{-1}; (d-f) Scaling factors of Col-FixOH; (g-i) Scaling factors of Prof-FixOH; (j-l) Scaling factors of Col-VarOH. The scaling factors are the ratios between a posteriori to a priori CO emissions.

https://doi.org/10.5194/egusphere-2025-5432
Preprint. Discussion started: 18 November 2025

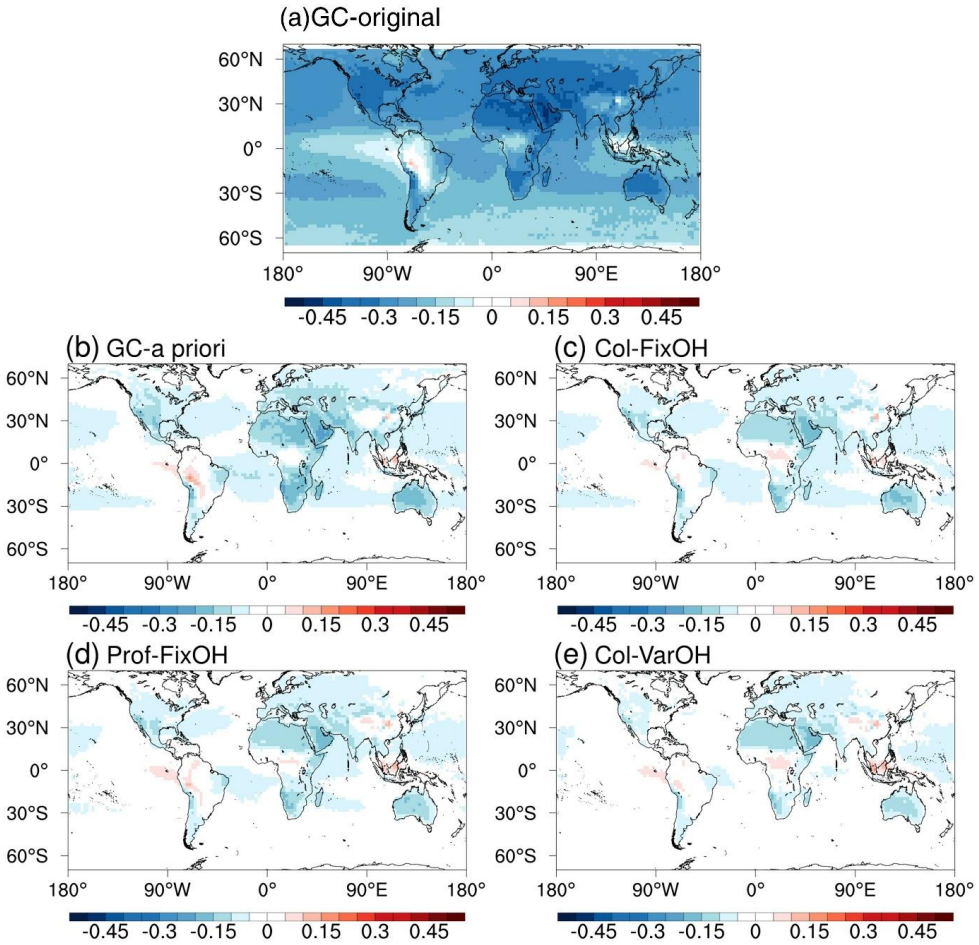

Fig. 2. Relative bias in column CO for 2003-2022, calculated as (Model - MOPITT) / MOPITT for GC-original (a), GC-a priori (b), and the a posteriori simulations (c-e).

https://doi.org/10.5194/egusphere-2025-5432
Preprint. Discussion started: 18 November 2025

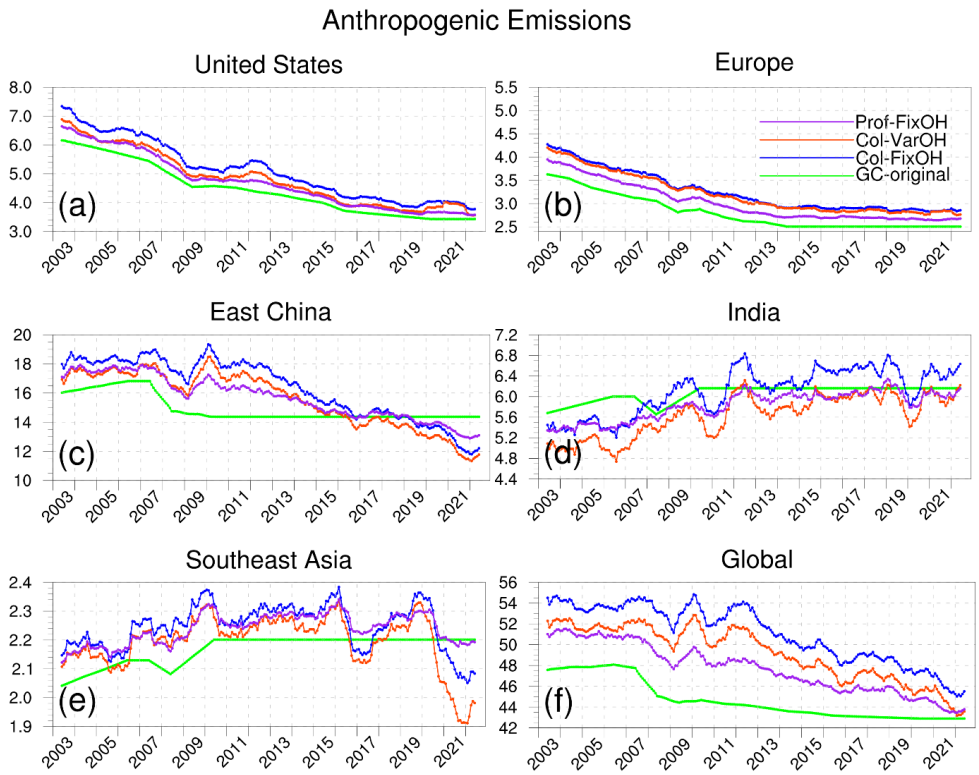

Fig. 3. Twelve-month moving average of anthropogenic CO emissions (Tg month^{-1}) in 2003-2022. The series includes the a priori emission (green) and the a posteriori emissions constrained with Col-FixOH (blue), Prof-FixOH (magenta) and Col-VarOH (red). The region definition is shown in Figure S1e.

https://doi.org/10.5194/egusphere-2025-5432
Preprint. Discussion started: 18 November 2025

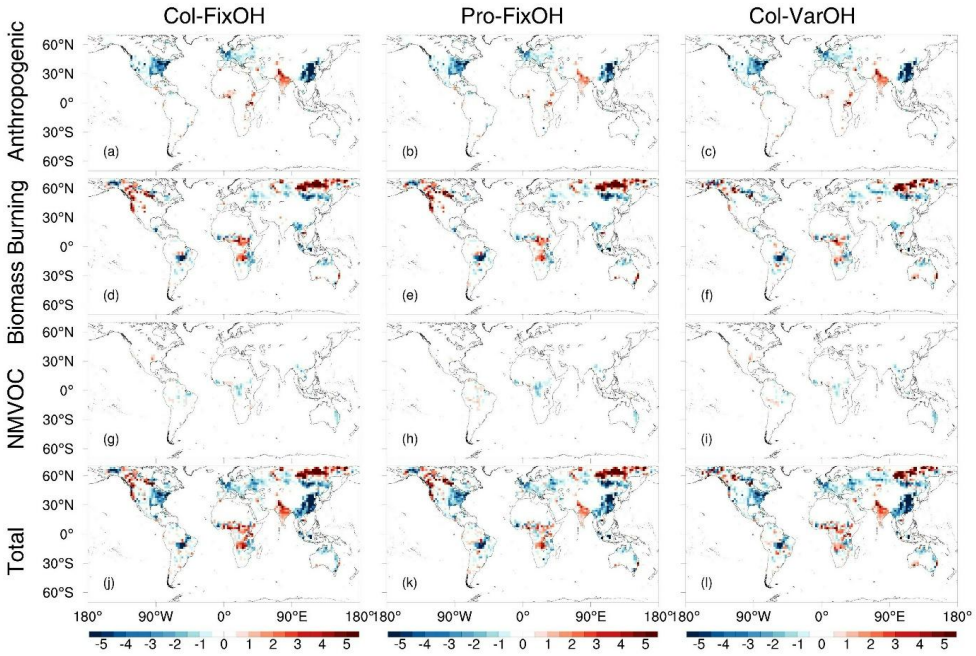

Fig. 4. Trends in CO emissions (10^{10} molecules cm^{-2} s^{-1} yr^{-1}) from 2003 to 2022, as constrained by different MOPITT data sets and OH configurations. Months where biomass burning CO emissions contributed >50% of the total emissions in a grid cell were excluded from the trend calculations for anthropogenic and biogenic VOC emissions.

https://doi.org/10.5194/egusphere-2025-5432
Preprint. Discussion started: 18 November 2025

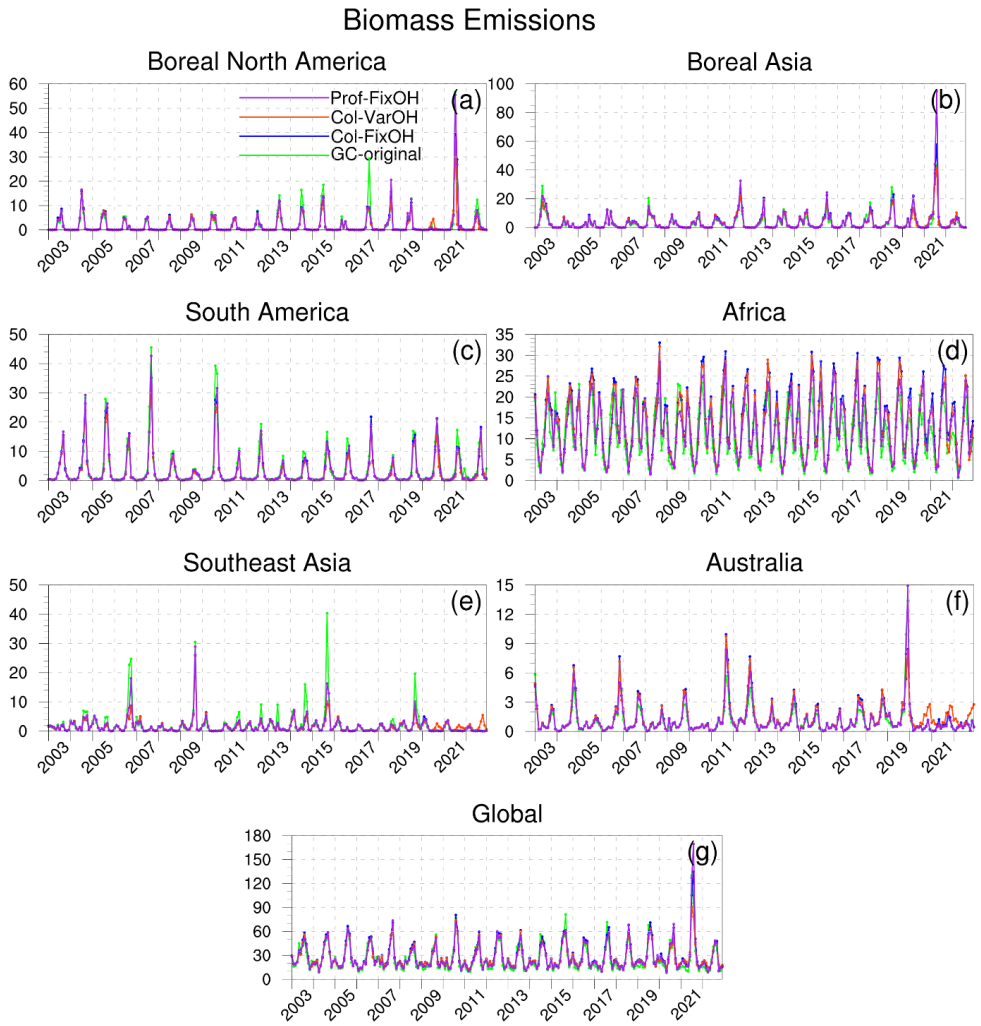

Fig. 5. Monthly biomass burning CO emissions (with unit Tg month^{-1}) in 2003-2022: a priori emission (green) and a posteriori emissions constrained with Col-FixOH (blue), Prof-FixOH (magenta) and Col-VarOH (red). The region definition is shown in Figure S1f.

https://doi.org/10.5194/egusphere-2025-5432
Preprint. Discussion started: 18 November 2025

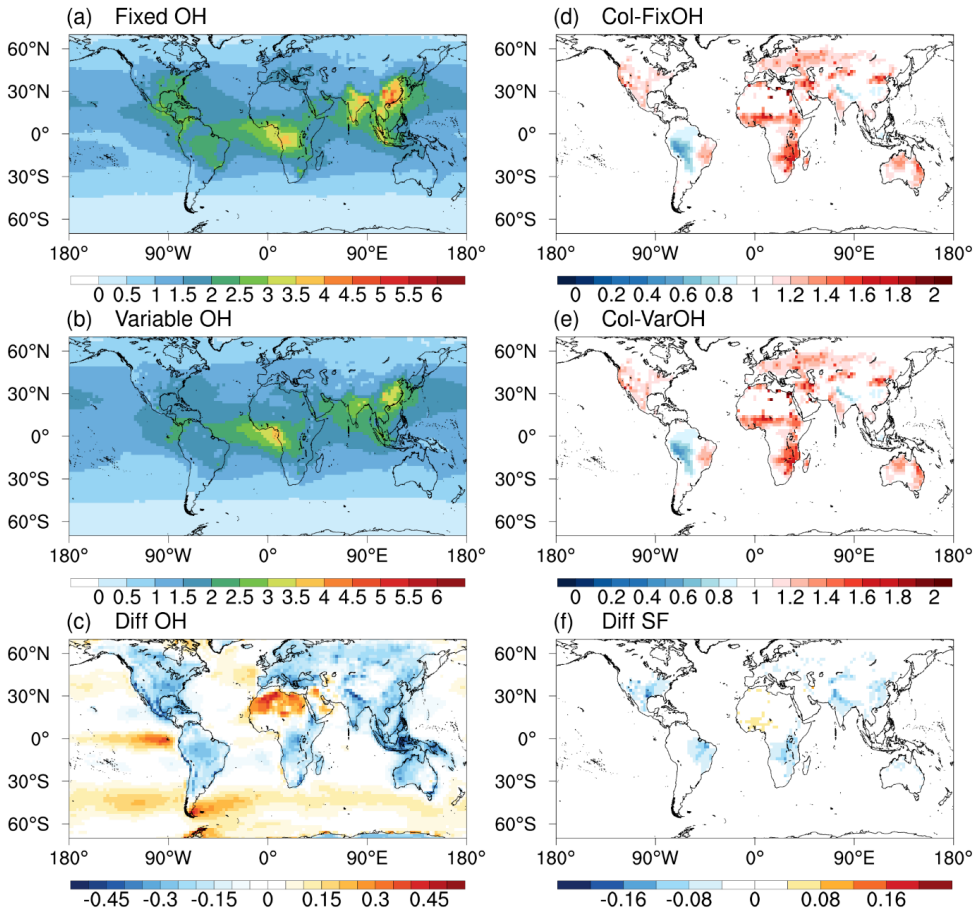

Fig. 6. Comparison of OH fields and their impact on emission estimates. (a-c) Tropospheric OH columns (10^{12} molecules cm^{-2}) averaged over 2003-2022 from (a) the fixed OH field, (b) the variable OH field, and (c) their difference (Variable - Fixed). (d-f) The corresponding CO emission scaling factors from (d) the Col-FixOH inversion, (e) the Col-VarOH inversion, and (f) the difference between them (Col-VarOH - Col-FixOH).

https://doi.org/10.5194/egusphere-2025-5432
Preprint. Discussion started: 18 November 2025

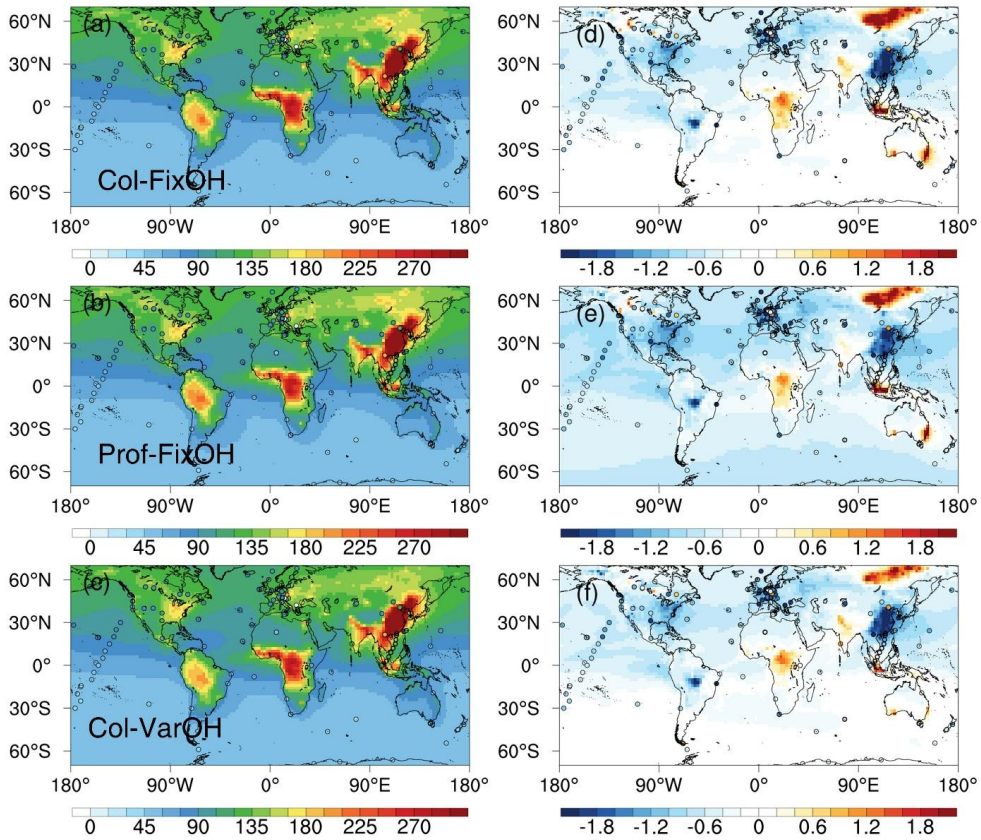

Fig. 7. (a-c) Mean surface CO concentrations (ppb) for 2003-2022 from WDCGG observations and model simulations. (d-f) Trend of surface CO concentration from observations and model simulations. Only stations with 20 year observations (the time range between the first and last observations) during 2003-2022 are included.

https://doi.org/10.5194/egusphere-2025-5432
Preprint. Discussion started: 18 November 2025

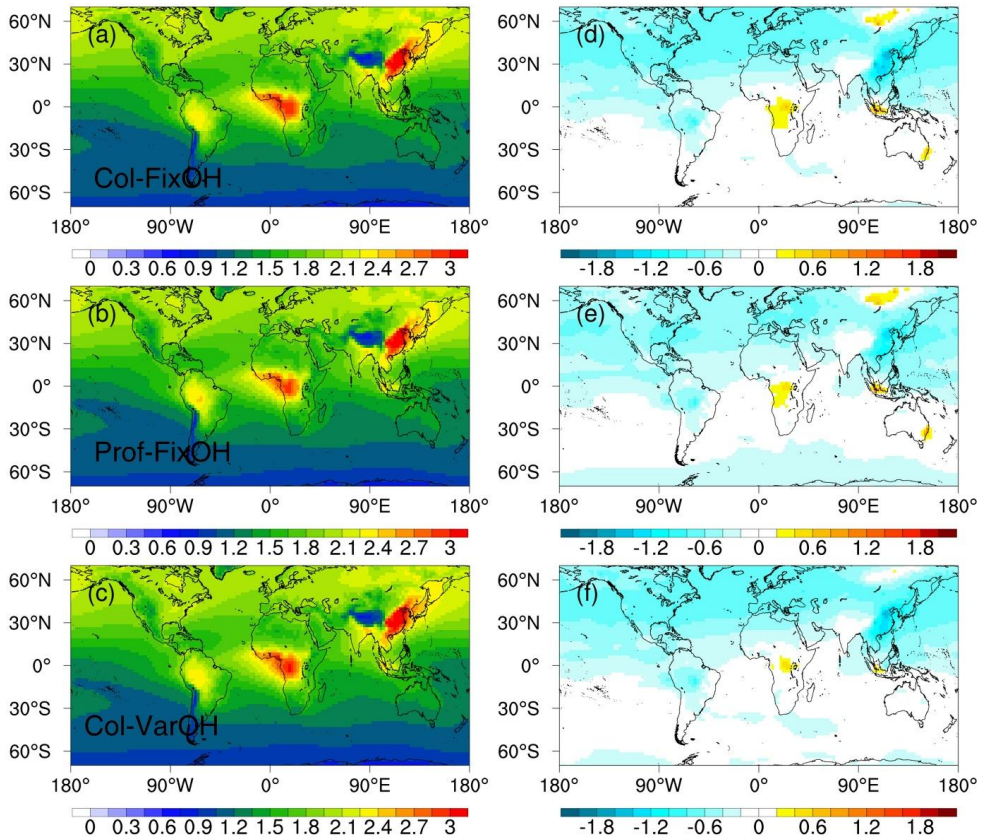

Fig. 8. (a-c) Mean modeled column CO concentrations (10^{18} molecules cm^{-2}) from 2003 to 2022. (d-f) Trend of modeled column CO concentrations (% yr^{-1}) from 2003 to 2022.

https://doi.org/10.5194/egusphere-2025-5432
Preprint. Discussion started: 18 November 2025

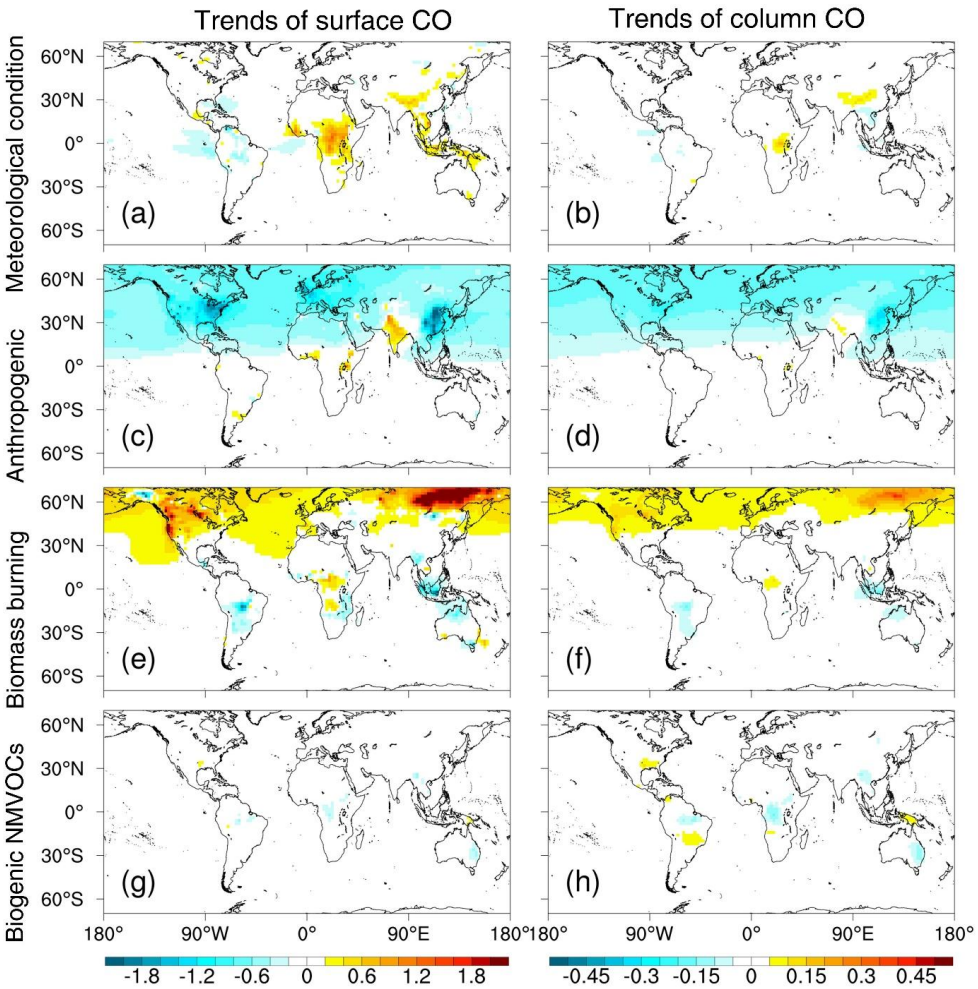

Fig. 9. Attribution of trends (% yr^{-1}) in surface and column CO from 2003 to 2022 to specific emission sectors, based on sensitivity simulations. Trends are shown for scenarios with: (a, b) all emissions fixed at 2003 levels; (c, d) only anthropogenic emissions varying over time; (e, f) only biomass burning emissions varying; (g, h) only biogenic VOC emissions varying. The varying emissions in these scenarios are prescribed from the Col-FixOH a posteriori inversion.